


Ferroelectric heterobilayer with tunable first- and higher-order topological statesRunhan Li, Ning Mao, Linke Cai, Yingxi Bai, Baibiao Huang, Ying Dai,^{*} and Chengwang Niu[†]
School of Physics, State Key Laboratory of Crystal Materials, Shandong University, Jinan 250100, China (Received 10 January 2023; revised 24 July 2023; accepted 29 August 2023; published 8 September 2023)

As conceptual milestones of nontrivial phenomenon, \mathbb{Z}_2 topological insulators (TIs) and higher-order TIs (HOTIs) have greatly reshaped the landscape of fundamental physics and materials. However, despite the exciting progress, a tunable topological phase transition between \mathbb{Z}_2 TIs and HOTIs remains elusive. Here, using a tight-binding model and first-principles calculations, we propose that ferroelectric switching can be a straightforward and efficient way for engineering the \mathbb{Z}_2 TIs and HOTIs phases with strikingly different bulk-boundary correspondence. Remarkably, based on the Wannier charge centers, edge states, and corner states analysis, we identify the ferroelectric heterobilayer composed of MgAl_2Se_4 and In_2S_3 as a material candidate of the predicted topological phase transition. Obviously, the ferroelectric switching opens up a technological avenue to bridge the first- and higher-order topologies with high possibility of innovative applications in topotronic and ferroelectric devices.

DOI: [10.1103/PhysRevB.108.125302](https://doi.org/10.1103/PhysRevB.108.125302)

Recent decades have witnessed a rapidly growing interest in \mathbb{Z}_2 topological insulators (TIs) [1–3]. The key characteristic of a \mathbb{Z}_2 TI is nontrivial gapless edge states, which are required by the bulk-boundary correspondence, i.e., a d -dimensional \mathbb{Z}_2 TI has a $(d - 1)$ -dimensional topological boundary state emerging on the surfaces or edges of the materials [4–6]. In recent studies, the topological body-boundary correspondence has been further generalized, giving rise to the concept of higher-order TIs [7,8]. From this point of view, the \mathbb{Z}_2 TIs can be called as the first-order TIs, and the higher-order TIs (HOTIs) do not exhibit gapless states in the $(d - 1)$ -dimensional boundary, but in the $(d - n)$ -dimensional boundary, e.g., gapless hinge or corner states, where $n > 1$. Indeed, as many efforts have been carried out, a number of electronic material candidates for the HOTIs have been proposed, but the experimental observations are only reported in three dimensions [7,9–21].

With rapidly growing enrichment of discovered topological materials, the study of topological phase transitions has become popular and attracted more and more attention in recent years [22,23]. Strain, electric field, temperature manipulation, etc., are important techniques to induce topological phase transitions and practical applications derived from them [24–28]. However, most of the proposed topological phase transitions, especially in two-dimensional (2D) materials, are between the trivial topology and the first-order one, whereas the phase transitions between the first-order topology and the higher-order topology are rarely reported [6]. In addition, most of the approaches to modulate the topological phase transitions mentioned above require the continuous application of an external field, implying that the topological state after removing the external field is volatile [24,26].

Manipulation in ferroelectric heterostructures has recently been reported as a nonvolatile modification approach that can eliminate continuous energy consumption [29,30]. 2D ferroelectrics, which possess unique switchable polarizations combined with plentiful material characteristics, are expected to play a dominant functional role in future nanoscale devices, such as field-effect transistors and ferroelectric random-access memory [31,32]. Remarkably, it has been experimentally demonstrated that the ferroelectric polarization in some 2D lattices, such as In_2S_3 [33], can be sufficiently strong and stable to hold promise for practical applications even at room temperature.

In this work, we demonstrate that heterobilayer $\text{MgAl}_2\text{Se}_4/\text{In}_2\text{S}_3$ yields coupling of the topological states and ferroelectricity, where the reversal of nonvolatile ferroelectric polarization induces a topological phase transition between the first-order \mathbb{Z}_2 TI and HOTI. Based on first-principles calculations, we determine the existence of nontrivial topological states by evaluating the \mathbb{Z}_2 invariant, gapless edge states, and nontrivial corner states. A tight-binding (TB) model for heterobilayers is constructed to demonstrate the feasibility of attaining the proposed topological phase transition. Our results enrich the topological phenomena and expand the coupling of topology and ferroelectrics, contributing to the development of a new generation of spintronics and ferroelectric devices.

The first-principles calculations are performed based on the density-functional theory using the projector augmented wave method as implemented in the Vienna *ab initio* simulation package (VASP) [34,35]. The generalized gradient approximation (GGA) of Perdew-Burke-Ernzerhof (PBE) is used for the exchange-correlation potential [36]. The cutoff energy is fixed to 450 eV, and all structures are relaxed until the residual forces are less than 0.01 eV/Å. The van der Waals (vdw) corrections are included by the DFT-D3 method [37]. Maximally localized Wannier functions (MLWFs) are constructed using the Wannier90 code [38].

^{*}daiy60@sdu.edu.cn[†]c.niu@sdu.edu.cn

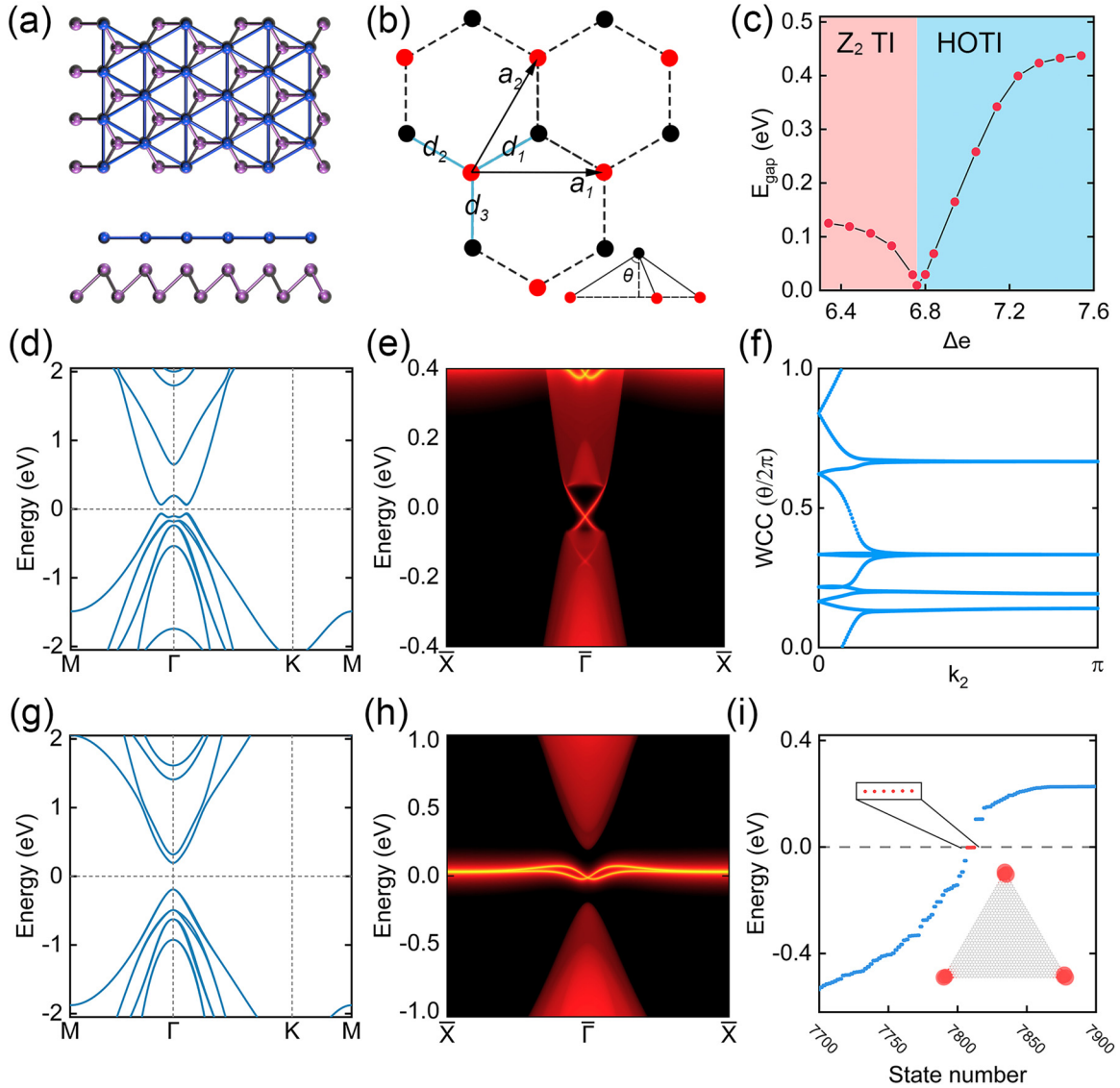


FIG. 1. (a) Top and side views of the TB model. The blue and light green spheres represent flat-layer and buckled-layer atoms, respectively. (b) Lattice of the lower monolayer, where red and black circles represent atoms at different heights. a_1 and a_2 are lattice vectors. d_1 , d_2 , and d_3 are the vectors that connect intralayer nearest-neighbor atoms. (c) Phase diagram of the TB model as energy offset Δe is varied, where the red and blue regions represent the \mathbb{Z}_2 TI and HOTI, respectively. Band structures of TB model with energy offset (d) $\Delta e = 6.39$ and (g) $\Delta e = 7.21$. The corresponding topological edge spectrum with (e) $\Delta e = 6.39$ and (h) $\Delta e = 7.21$. (f) Evolution of the WCC with energy offset $\Delta e = 6.39$ along k_2 . (i) Energy spectrum of a triangular nanoflake for the TB model with SOC, where the occupied corner states are marked by red dots. Inset shows the total charge distribution of the six corner states.

The higher-order corner states can be achieved in the 2D \mathbb{Z}_2 TIs by applying an in-plane Zeeman field, where the 2D \mathbb{Z}_2 TIs are destroyed because the time-reversal symmetry is broken, i.e., realizing only the magnetic HOTIs [39,40]. In this work, we have accomplished the attainment of a phase transition between the 2D \mathbb{Z}_2 TI and HOTI phases induced by ferroelectric switching, without the introduction of an external magnetic field. To establish the existence of the predicted topological phase transition, we start our discussion with the Slater-Koster TB model on a 2D honeycomb heterobilayer, which consists of a flat monolayer (upper layer) and a buckled monolayer (lower layer), as shown in Figs. 1(a) and 1(b) [41,42]. The $p_x/p_y/p_z$ orbitals localized on the lower buckled layer and the p_x/p_y orbitals localized on the upper

flat layer are considered to construct our TB model, and, in addition, to show the ferroelectric polarization, s orbitals of the inner atoms of the buckled layer are employed (calculation details of the TB model are provided in Appendix A). Taking into consideration of all the interlayer and intralayer nearest-neighbor interactions, the Hamiltonian can be expressed as

$$H_0(\mathbf{k}) = \begin{bmatrix} h_{11} & h_{12} & \cdots & h_{19} \\ h_{12}^* & h_{22} & & h_{29} \\ \vdots & & \ddots & \vdots \\ h_{19}^* & h_{29}^* & \cdots & h_{99} \end{bmatrix}, \quad (1)$$

and the onsite spin-orbit coupling (SOC) interaction is introduced by the atomic term $L_z S_z$ as

$$H_{\text{SOC}} = \lambda_{\text{SOC}} L_z S_z, \quad (2)$$

with λ_{SOC} denoting the strength of onsite SOC. In the absence of SOC, $\lambda_{\text{SOC}} = 0$, the system is gapless and shows a semimetallic character with the band crossing at the Γ point, a band gap opens when switching the SOC on, as illustrated in Fig. 1(d). Since the model is protected by the time-reversal symmetry, we expect the appearance of the 2D \mathbb{Z}_2 TI phase with Quantum Spin Hall (QSH) effect [4]. As displayed in Figs. 1(e) and 1(f), the topologically nontrivial nature can be explicitly confirmed by the emergence of gapless edge states in the semi-infinite nanoribbons, and the calculations of Wannier charge center (WCC) which acquire a nonzero value of $\mathbb{Z}_2 = 1$.

To uncover the nontrivial topological phase transition, the energy offset Δe between the p_x/p_y orbitals of the flat-up layer and the s orbitals of the inner atoms of buckled-down layer is used as a tuning parameter, and Fig. 1(c) presents the variation in the global energy gap as a function of Δe . Starting from the small Δe , it can be clearly seen that the global energy gap decreases rapidly with increasing Δe . Remarkably, a process of the energy gap closing and reopening occurs at $\Delta e = 6.76$, thus marking a topological phase transition from insulators with $\mathbb{Z}_2 = 1$ to that with $\mathbb{Z}_2 = 0$ as is confirmed by our topological analysis. Figures 1(g) and 1(h) show the bulk band structure and edge spectrum after the phase transition. The gapless edge states disappear and a pair of floating edge states appear in the bulk band gap, which is often considered as an important signature of the HOTIs. To identify the band topology, we construct a triangular nanoflake of the TB model with C_3 rotational symmetry and present the energy spectrum in Fig. 1(i). For the spinful system with SOC, six continuous energy states (red dot) emerge at the Fermi level. The total spatial distributions of wave functions for these six states are present in the inset of Fig. 1(i), where the electrons accumulate mainly on the corners of the triangular nanoflake and there is almost no electron distribution in the internal part of the triangular nanoflake, indicating that the HOTIs as well as the topological phase transition between the first-order \mathbb{Z}_2 TIs and HOTIs are achieved.

After introducing a simplified tight-binding model of the key idea in the previous section, we now show that this idea can in principle be realized in an actual physical system. We investigate real heterobilayer materials constructed from some big band-gap 2D semiconductors and van der Waals materials In_2X_3 ($X=\text{S}, \text{Se}$) which are well-known 2D ferroelectric semiconductors with properties of high light sensitivity and fast response [43–46]. As an example, we apply our approach to the $\text{MgAl}_2\text{Se}_4/\text{In}_2\text{S}_3$ heterobilayers (see Appendix A). The MgAl_2Se_4 monolayers have been reported to have high in-plane electron mobility, making it suitable for n -type field-effect transistors [47]. Additionally, the monolayer MgAl_2Se_4 has appropriate band-gap and band-edge alignment, which makes it a potential photocatalyst for water splitting [47,48]. In addition, the In_2S_3 , with a buckled honeycomb lattice, is theoretically predicted to be out-of-plane polarized ferroelectric, as shown in Fig. 2(a), originating from a noncentrosymmetric lattice structure [33,43–45,49–

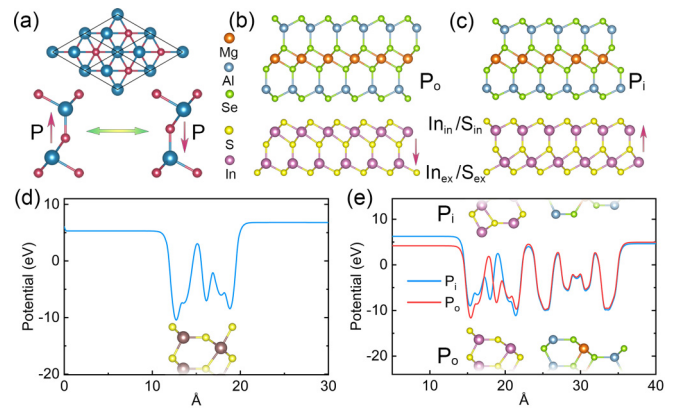


FIG. 2. (a) Top view of the crystal structure for In_2S_3 monolayer, and schematic diagrams of the two polarization states. Red arrows denote the polarization directions. Side views of the $\text{MgAl}_2\text{Se}_4/\text{In}_2\text{S}_3$ heterobilayer with (b) outward polarization P_o and (c) inward polarization P_i . The inner and exterior In/S layer are labeled as $\text{In}_{in}/\text{S}_{in}$ and $\text{In}_{ex}/\text{S}_{ex}$, respectively. Plane-averaged electrostatic potential of (d) In_2S_3 monolayer and (e) heterobilayers with the blue and red lines representing inward and outward polarized states, respectively.

52]. Moreover, the In_2S_3 has been extensively researched for applications such as ultrathin 2D photo detection, second harmonic generation, and piezoelectric devices. Moreover, the In_2S_3 has been extensively researched for applications such as ferroelectric memory, photoelectrics, and thermoelectrics [51,53]. The MgAl_2Se_4 and In_2S_3 have lattice constants of $a = b = 3.92 \text{ \AA}$ and $a = b = 3.91 \text{ \AA}$, respectively [49,54], where the tiny difference in lattice parameters guarantee the high operability of constructing heterostructure.

As illustrated in Fig. 2(a), In_2S_3 is a quintuple-layered structure with the stacking order of S-In-S-In-S along the z direction, where movement of the middle S atoms can induce two different switchable ferroelectric states. After considering the van der Waals (vdw) corrections, total energies of various stacking configurations for two opposite polarizations have been investigated, and two most stable ferroelectric stacking configurations are found and used to confirm the practicability of our proposed topological phase transition. As shown in Figs. 2(b) and 2(c), when the middle S atoms shift downwards, the ferroelectric polarization (inward, P_i) points towards the MgAl_2Se_4 monolayer, where the bottom Se atom of MgAl_2Se_4 monolayer is precisely above the top In atom of the In_2S_3 in the z direction, while when shift upwards, the ferroelectric polarization (outward, P_o) points in the opposite direction. After full geometric relaxation, P_o configuration has a layer spacing of 3.03 \AA , where the top atom of MgAl_2Se_4 monolayer is precisely above the middle S atom of the In_2S_3 monolayer in the z direction. And P_i configuration has a layer spacing of 3.11 \AA , where the bottom Se atom of MgAl_2Se_4 monolayer and the top In atom of the In_2S_3 remain aligned in the z direction. Both configurations share the same $P3m1$ space group.

To get preliminary insight into the topological properties of the $\text{MgAl}_2\text{Se}_4/\text{In}_2\text{S}_3$ heterobilayers under both the polarizations P_i and P_o , we present in Fig. 3 the orbitally resolved

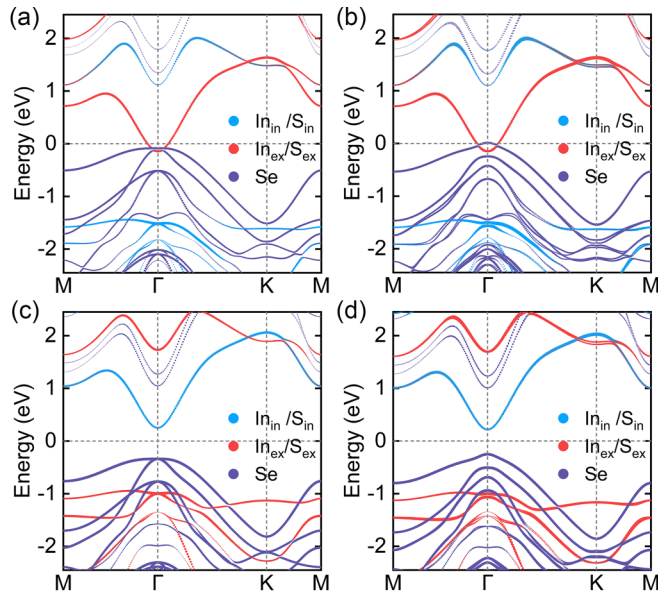


FIG. 3. Electronic band structures of the ferroelectric $\text{MgAl}_2\text{Se}_4/\text{In}_2\text{S}_3$ heterobilayers under outward polarization (a) without SOC and (b) with SOC, and under inward polarization (c) without SOC and (d) with SOC, respectively. Inset shows enlarged view of band around the Fermi level. The color represents the contribution of Sb layer, inner In/S layer ($\text{In}_{in}/\text{S}_{in}$), and exterior In/S layer ($\text{In}_{ex}/\text{S}_{ex}$).

band structures without and with SOC. It is clearly visible that band structures of the two ferroelectric configurations are significantly different, meaning that the electronic bands can indeed be tuned by the ferroelectric switching due to when the plane-averaged electrostatic potential is clearly varied. To visualize it, Fig. 2(e) plots the plane-averaged electrostatic potential as a function of the vertical coordinate z across the ferroelectric heterobilayers. Neglecting the slight potential difference on the right side, the static potential difference between the two ferroelectric structures on the left side is approximately 2.06 eV. This value is in close proximity to the band shift observed at Γ , as illustrated in Figs. 3(a) and 3(c). For the outward-polarized configuration P_o , in the absence of SOC as shown in Fig. 3(a), energy bands with the Se atom orbitals $\text{In}_{ex}/\text{S}_{ex}$ are crossing at the Γ point, exhibiting the Dirac cone-like features. Switching on SOC leads to the band gap opening with a magnitude of 27.4 meV, which is an important mechanism for the formation of a topologically nontrivial phase. However, the band gap for the inward-polarized configuration P_i is 0.588 eV in the case without SOC, and the valence band maximum is dominated by the Sb orbital while the conduction band minimum is dominated by the inner In/S orbital ($\text{In}_{in}/\text{S}_{in}$), respectively. When SOC is switched on, the band gap decreases to 0.467 eV and the orbital contributions around the valence band maximum and conduction band minimum remain the same as that without SOC, i.e., no SOC-induced band inversion takes place, and

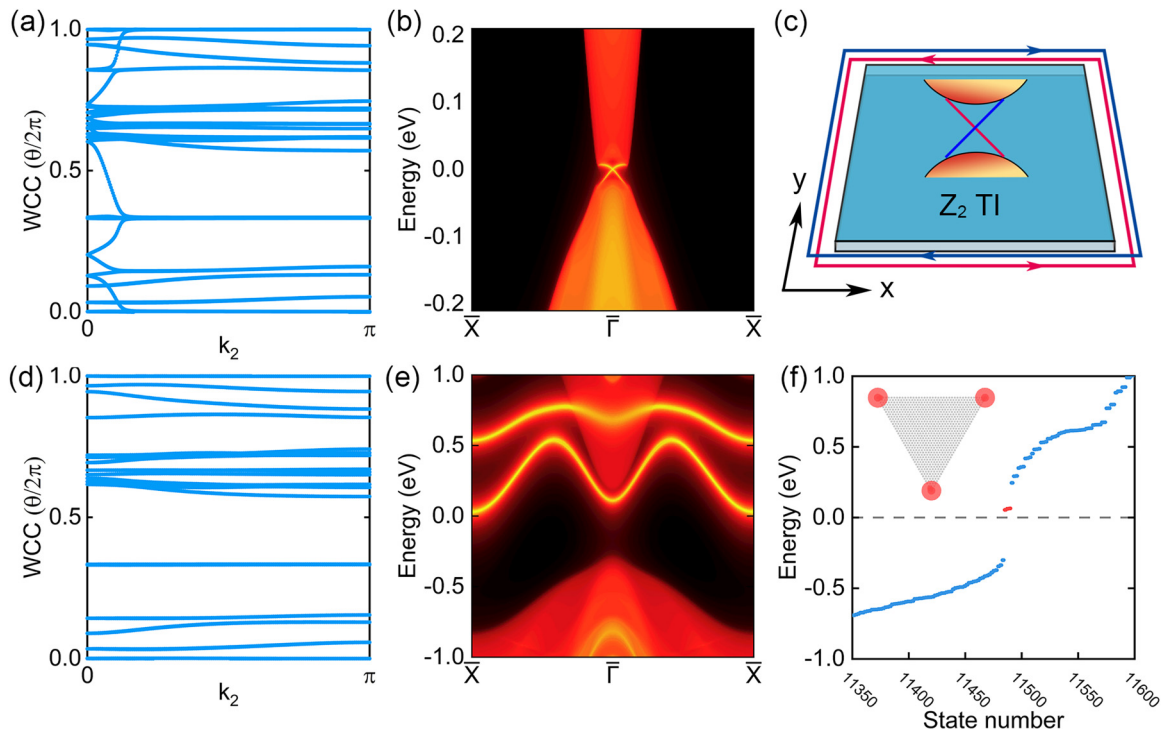


FIG. 4. Evolution of WCC for $\text{MgAl}_2\text{Se}_4/\text{In}_2\text{S}_3$ heterobilayers with (a) outward polarization and (d) inward polarization. The corresponding topological edge spectrum with (b) outward polarization and (e) inward polarization. (c) Illustration of the 2D \mathbb{Z}_2 TI and the helical edge states on the boundary. (f) Energy spectrum and charge distributions of C_3 -symmetric triangle-shaped nanoflake for the $\text{In}_2\text{S}_3/\text{Sb}$ heterobilayer with inward polarization, where the occupied corner states are marked by red dots.

TABLE I. The lattice constants a_0 , Å and band gap E_g (eV) and the value of \mathbb{Z}_2 invariant of four candidate heterobilayers capable of exhibiting the topological phase transition from first-order \mathbb{Z}_2 TIs to HOTIs are presented. Results are given for both outward P_o and inward P_i polarizations.

Compounds	a_0	$E_g(P_o)$	$E_g(P_i)$	$\mathbb{Z}_2(P_o)/\mathbb{Z}_2(P_i)$
MgAl ₂ Se ₄ /In ₂ S ₃	3.91	0.0274	0.4674	1/0
Cu ₂ Br ₄ /In ₂ S ₃	3.93	0.0228	0.7807	1/0
Sb/In ₂ Se ₃	4.06	0.0263	0.4511	1/0
Cu ₂ I ₂ /In ₂ Se ₃	4.14	0.0454	0.2963	1/0

thus MgAl₂Se₄/In₂S₃ under P_i polarization cannot be a 2D \mathbb{Z}_2 TI.

Figure 4(a) presents the evolution of WCC for MgAl₂Se₄/In₂S₃ heterobilayers with polarization P_o ; clearly the number of crossings between the WCC and a reference horizontal line is odd, displaying a nontrivial topological index $\mathbb{Z}_2 = 1$, and thus confirming the 2D \mathbb{Z}_2 TI nature for MgAl₂Se₄/In₂S₃ heterobilayers with P_o . To reveal the bulk-boundary correspondence, the edge Green's function of the semi-infinite system is obtained by using the iterative method and the MLWFs, and the resulted local density of states is depicted in Fig. 4(b). One can clearly see a pair of gapless edge states within the energy window of the SOC gap, which is in direct agreement with the nontrivial value of $\mathbb{Z}_2 = 1$.

In contrast to P_o , as illustrated in Fig. 4(d), the \mathbb{Z}_2 index computed by WCC for MgAl₂Se₄/In₂S₃ heterobilayers with polarization P_i is $\mathbb{Z}_2 = 0$. This is a natural consequence of no SOC-induced band inversion as discussed above. Consequently, there is no gapless edge states connecting the conduction and valence bands, but floating edge states emerge in the band gap, as shown in Fig. 4(e). To check the HOTI phase and the ferroelectric-switched topological phase transition, a triangular nanoflake with C_3 is calculated using the MLWFs method with SOC and the results are plotted in Fig. 4(f). Six continuous energy states (red dots) emerge near the Fermi level and the corresponding electrons accumulate mainly on the corners of the triangular nanoflake. The eigenvalues of threefold rotation symmetry of the occupied energy bands at the high-symmetric points can be used to define the nontrivial topological indices for HOTIs. The eigenvalues of threefold rotation symmetry at high-symmetric points are denoted as $\Sigma_m^{(3)} = e^{2\pi i(m-1)/3}$, where $m = 1, 2, 3$. The integer topological invariants are defined by comparing the rotation eigenvalues of the occupied bands at the Σ point to the Γ point, i.e., $[\Sigma_m^{(3)}] \equiv \#\Sigma_m^{(3)} - \#\Gamma_m^{(3)}$, where $\#\Sigma_m^{(3)}$ ($\#\Gamma_m^{(3)}$) is the number of the occupied bands with eigenvalue $\Sigma_m^{(3)}$ ($\Gamma_m^{(3)}$) [8,17]. The topological indices $\chi^{(3)}$ are then obtained from $\chi^{(3)} = ([K_1^{(3)}], [K_2^{(3)}])$, where the superscript 3 of $\chi^{(3)}$ labels the C_3 symmetry. The calculated nonzero topological index of $\chi^{(3)} = (-4, 1)$, together with the spatial distribution of wave functions for corner states, confirms that the inward-polarized heterobilayer is a HOTI.

To confirm the universality of our ferroelectric modulated topological phase transition approach, we searched for stable 2D materials with large band gaps and lattice parameters similar to In₂X₃ (X=S, Se) monolayers to construct hetero-

TABLE II. The parameter amplitudes in eV of the Slater-Koster TB model with SOC.

ε_x^u $V_{sp\sigma}^u$	ε_s^l $V_{pp\sigma}^i$	ε_x^l $V_{pp\pi}^l$	ε_z^l $V_{pp\pi}^l$	$V_{pp\sigma}^u$ $V_{pp\pi}^i$	$V_{ss\sigma}^l$ θ	$V_{pp\sigma}^l$ λ_{soc}^i	$V_{sp\sigma}^l$ λ_{soc}^l
-3.54	2.85/3.67	1.00	-0.4	1.10	-0.48	2.4	0.05
0.01	0.05	0.08	-0.66	0.05	54°	0.2	0.5* λ_{soc}^u

bilayers. The main challenge was creating band inversion in the P_o phase after considering SOC. We finally screened four candidate materials to address this challenge. In Table I, we list four candidate heterobilayers along with their structural parameters and their band information of the two ferroelectric phases. Detailed computational results for other candidate materials are included in Appendix A.

In summary, we have presented a heterobilayer TB model for 2D honeycomb lattice that can realize the exotic topological phase transition between the first-order \mathbb{Z}_2 TIs and HOTIs. Remarkably, on the basis of first-principles calculations, we uncovered that the ferroelectric heterobilayer MgAl₂Se₄/In₂S₃ and several other candidate materials can realize both the 2D \mathbb{Z}_2 TI and HOTI phases with opposite polarizations, i.e., the proposed topological phase transition via ferroelectric switching. This phase transition strategy is deserving of further study because it is not unique to the used material MgAl₂Se₄/In₂S₃ and can be implemented to other suitable ferroelectric multilayers. Our results not only demonstrate the strong coupling of several topological phases and ferroelectricity in two-dimensional materials, but also offer an intriguing analytical framework for ferroelectric topological materials, enrich and supplement the research in the field of topological phase transitions, and facilitate the development and application of multifunctional nanodevices.

This work was supported by the National Natural Science Foundation of China (Grants No. 12174220, No. 12074217, and No. 11904205), the Shandong Provincial Natural Science Foundation of China (Grants No. ZR2019QA019 and No. ZR2019MEM013), the Shandong Provincial Key Research and Development Program (Major Scientific and Technological Innovation Project) (Grant No. 2019JZZY010302), and the Qilu Young Scholar Program of Shandong University.

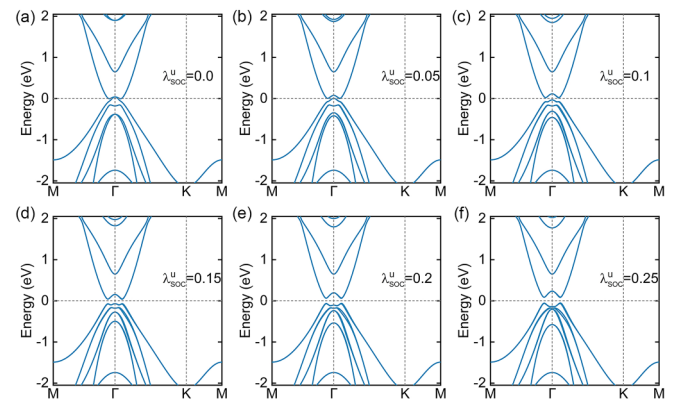


FIG. 5. The band structures of TB model with energy offset $\Delta e = 6.39$ for difference magnitude of onsite SOC hopping term λ_{soc}^u , from 0.0 to 0.25.

APPENDIX A: DETAILED ANALYSIS FOR THE TIGHT-BINDING MODEL

We start our discussion with a Slater-Koster TB model on a 2D honeycomb heterobilayer. This 2D honeycomb heterobilayer consists of a flat monolayer (upper layer) and a buckled monolayer (lower layer), as shown in Figs. 1(a) and 1(b). The model is composed of p orbitals localized on the buckled layer, s -like orbitals of the inner atoms of the buckled layer, and p_x/p_y orbitals localized on the flat layer for a total of nine orbitals. For simplicity, we ignore the spin variables,

which means that these terms are identical in terms of spin degrees of freedom. Taking into consideration all interlayer and intralayer nearest-neighbor interactions, the Hamiltonian can be expressed as

$$H_0(\mathbf{k}) = \begin{bmatrix} h_{11} & h_{12} & \cdots & h_{19} \\ h_{12}^* & h_{22} & & h_{29} \\ \vdots & & \ddots & \vdots \\ h_{19}^* & h_{29}^* & \cdots & h_{99} \end{bmatrix}, \quad (\text{A1})$$

in which

$$\begin{aligned} h_{11} &= \varepsilon_x^l, & h_{22} &= \varepsilon_x^l, & h_{33} &= \varepsilon_z^l, \\ h_{44} &= \varepsilon_x^l, & h_{55} &= \varepsilon_x^l, & h_{66} &= \varepsilon_z^l, \\ h_{77} &= \varepsilon_s^l + 2(\cos(k_1) + \cos(k_1 - k_2) + \cos(k_2))V_{ss\sigma}^l, \\ h_{88} &= \varepsilon_x^u + \frac{1}{2}(\cos(k_1 - k_2) + \cos(k_2))(3V_{pp\pi}^l + V_{pp\sigma}^l) + 2\cos(k_1)V_{pp\sigma}^l, \\ h_{99} &= \varepsilon_x^u + \frac{1}{2}((4\cos(k_1) + \cos(k_1 - k_2) + \cos(k_2))V_{pp\pi}^l + 3(\cos(k_1 - k_2) + \cos(k_2))V_{pp\sigma}^l), \\ h_{14} &= \frac{1}{8}(((1 + e^{-ik_1})(3\cos(2\theta) + 5) + 8e^{-ik_2})V_{pp\pi}^u + 6e^{-ik_1}(1 + e^{ik_1})\sin^2(\theta)V_{pp\sigma}^u), \\ h_{15} &= -\frac{1}{4}\sqrt{3}e^{-ik_1}(-1 + e^{ik_1})\sin^2(\theta)(V_{pp\pi}^u - V_{pp\sigma}^u), \\ h_{16} &= -\frac{1}{4}\sqrt{3}e^{-ik_1}(-1 + e^{ik_1})\sin(2\theta)(V_{pp\pi}^u - V_{pp\sigma}^u), \\ h_{24} &= -\frac{1}{4}\sqrt{3}e^{-ik_1}(-1 + e^{ik_1})\sin^2(\theta)(V_{pp\pi}^u - V_{pp\sigma}^u), \\ h_{25} &= \frac{1}{8}((8e^{-ik_2}\cos^2(\theta) + (1 + e^{-ik_1})(\cos(2\theta) + 7))V_{pp\pi}^u + 2(e^{-ik_1} + 4e^{-ik_2} + 1)\sin^2(\theta)V_{pp\sigma}^u), \\ h_{26} &= -\frac{1}{2}\sin(\theta)\cos(\theta)(-i\sin(k_1) + 2i\sin(k_2) + \cos(k_1) - 2\cos(k_2) + 1)(V_{pp\pi}^u - V_{pp\sigma}^u), \\ h_{34} &= -\frac{1}{4}\sqrt{3}e^{-ik_1}(-1 + e^{ik_1})\sin(2\theta)(V_{pp\pi}^u - V_{pp\sigma}^u), \\ h_{35} &= -\frac{1}{2}\sin(\theta)\cos(\theta)(-i\sin(k_1) + 2i\sin(k_2) + \cos(k_1) - 2\cos(k_2) + 1)(V_{pp\pi}^u - V_{pp\sigma}^u), \\ h_{36} &= (-i(\sin(k_1) + \sin(k_2) + i) + \cos(k_1) + \cos(k_2))(\sin^2(\theta)V_{pp\pi}^u + \cos^2(\theta)V_{pp\sigma}^u), \\ h_{47} &= -\frac{1}{2}\sqrt{3}\sin(\theta)V_{sp\sigma}^l(-i\sin(k_1) + \cos(k_1) - 1), \\ h_{48} &= \frac{1}{2}(\cos(k_1 - k_2) + \cos(k_2))(3V_{pp\pi}^i + V_{pp\sigma}^i) + 2\cos(k_1)V_{pp\sigma}^i, \\ h_{49} &= \frac{1}{2}\sqrt{3}(\cos(k_1 - k_2) - \cos(k_2))(V_{pp\pi}^i - V_{pp\sigma}^i), \\ h_{57} &= \frac{1}{2}(e^{-ik_1} - 2e^{-ik_2} + 1)\sin(\theta)V_{sp\sigma}^l, \\ h_{58} &= \frac{1}{2}\sqrt{3}(\cos(k_1 - k_2) - \cos(k_2))(V_{pp\pi}^i - V_{pp\sigma}^i), \\ h_{59} &= \frac{1}{2}((4\cos(k_1) + \cos(k_1 - k_2) + \cos(k_2))V_{pp\pi}^i + 3(\cos(k_1 - k_2) + \cos(k_2))V_{pp\sigma}^i), \\ h_{67} &= -\frac{1}{2}\sqrt{3}\sin(\theta)(-i\sin(k_1) + \cos(k_1) - 1)V_{sp\sigma}^l, \\ h_{78} &= i(2\sin(k_1) + \sin(k_1 - k_2) + \sin(k_2))V_{sp\sigma}^i, \\ h_{79} &= -i\sqrt{3}(\sin(k_1 - k_2) - \sin(k_2))V_{sp\sigma}^i, \\ h_{89} &= \frac{1}{2}\sqrt{3}(\cos(k_1 - k_2) - \cos(k_2))(V_{pp\pi}^l - V_{pp\sigma}^l), \end{aligned}$$

where $\varepsilon_x^u, \varepsilon_s^l, \varepsilon_x^l, \varepsilon_z^l$ are onsite energies for p_x/p_y orbitals of upper layer and s orbital, p_x/p_y orbital, p_z orbitals of lower layer, respectively; $V_{pp\sigma}^u, V_{ss\sigma}^l, V_{pp\sigma}^l, V_{sp\sigma}^l$, and $V_{sp\sigma}^i, V_{pp\sigma}^i$ are σ type hopping energies; $V_{pp\pi}^u, V_{pp\pi}^l$, and $V_{pp\pi}^i$ is π -type hopping energies, where u, l and i represent the intralayer

nearest-neighbor interactions hopping for upper layer and lower layer and the interlayer nearest-neighbor interactions hopping between upper layer and lower layer; θ is the buckling angle between z axis and the vector that connects the two orbitals for lower layer. For the interlayer nearest-neighbor

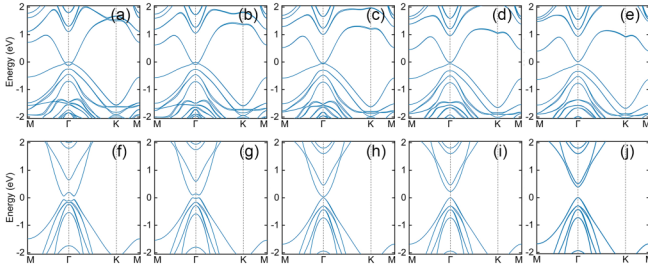


FIG. 6. [(a)–(e)] The band structure evolution of $\text{MgAl}_2\text{Se}_4/\text{In}_2\text{S}_3$ heterobilayer during the transition from P_o phase to P_i phase with SOC. The band crossing and reopening process is clearly shown. [(f)–(j)] The band structures of TB model with SOC for different magnitude of energy offset Δe , from 6.39 to 7.21.

interactions hopping between upper layer and lower layer, we can reasonably simplify the coefficients related to the z direction angle by the equation $V^i = V^0 \cos(\varphi)$, where φ is the angle between the plane of one monolayer and the vector that connects the two orbitals, and V^0 is actual hopping strength. The other upper triangular matrix elements that do not appear are zero. The energy offset Δe between onsite energies for p_x/p_y orbitals of upper layer and s orbital of lower layer are given by $\Delta e = \varepsilon_s^l - \varepsilon_x^u$. For simplicity we drop the spin variable, meaning that the terms are identical and diagonal in the spin degree of freedom. The parameters of the TB model are presented in Table II.

Then we consider SOC interaction by the atomic term $L \times S$, we get the total Hamiltonian as

$$H = H_0 + H_{\text{soc}}, \quad (\text{A2})$$

in which

$$H_{\text{soc}} = \lambda_{\text{soc}}^{u/d} L \times S, \quad (\text{A3})$$

where $\lambda_{\text{soc}}^{u/l}$ is onsite SOC interaction strength for upper layer and lower layer. The energy bands of the TB model with different SOC strengths can be seen in Fig. 5.

The higher-order corner states arise from the p orbitals of the buckled-down honeycomb layer in the TB model, while the p orbitals of the honeycomb layer In_2S_3 in the heterobilayer also contribute to the higher-order topological properties. On the other hand, during the ferroelectric reversal process, there is a band inversion between the s orbitals of the layer In_2S_3 and the p_x/p_y orbitals of the layer MgAl_2Se_4 , leading to a phase transition from higher-order to first-order topological states. In this TB model, we introduce the s orbitals on the buckled-down honeycomb layer and the p_x/p_y orbitals on the flat-up layer to capture this transition process. In Fig. 3, the band analysis at the Γ point reveals a significant change in the energy difference between the bands contributed by the $\text{In}_{\text{ex}}/\text{S}_{\text{ex}}$ s orbitals (marked in red) and the bands contributed by the Se p orbitals during the ferroelectric transition. This change corresponds to the modulation of the energy offset Δe between the s orbitals of the buckled-down layer and the p_x/p_y orbitals of the flat-up layer defined in our model. In Figs. 6(a)–6(e), the band structure evolution during the ferroelectric phase transition from the P_o phase to the P_i phase for the $\text{MgAl}_2\text{Se}_4/\text{In}_2\text{S}_3$ heterobilayer is displayed. Due to the small interlayer spacing difference between the two ferroelectric phases, we maintain a constant interlayer spacing during the phase transition. Along the ferroelectric switching path, we constructed 17 intermediate structures. Near the P_o phase, we observed a band inversion process, which is in good agreement with the band evolution obtained by adjusting the parameter Δe in the TB model, as shown in Figs. 6(f)–6(j). The TB model enables us to represent this ferroelectric phase transition by adjusting the parameter Δe ,

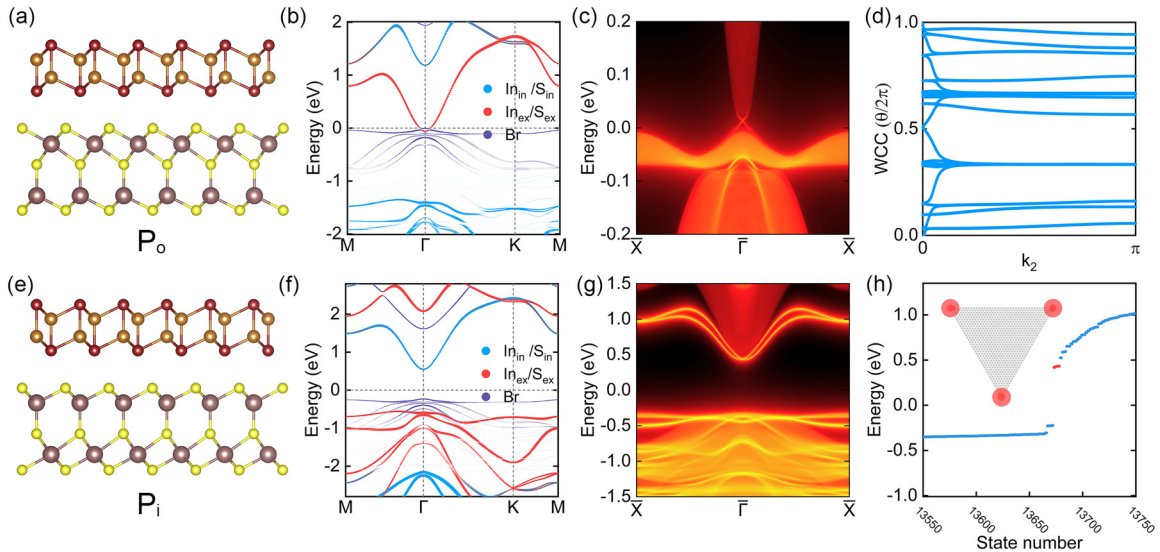


FIG. 7. Side views of the $\text{Cu}_2\text{Br}_2/\text{In}_2\text{S}_3$ heterobilayer with (a) outward polarization P_o and (c) inward polarization P_i . Electronic band structures of the $\text{Cu}_2\text{Br}_2/\text{In}_2\text{S}_3$ heterobilayer (b) under outward polarization with SOC, and (f) under inward polarization with SOC, respectively. The corresponding topological edge spectrum with (c) outward polarization and (g) inward polarization. (d) Evolution of WCC for $\text{Cu}_2\text{Br}_2/\text{In}_2\text{S}_3$ heterobilayer with outward polarization. (h) Energy spectrum and charge distributions of triangle-shaped nanoflake for the heterobilayer with inward polarization, where the occupied corner states are marked by red dots.

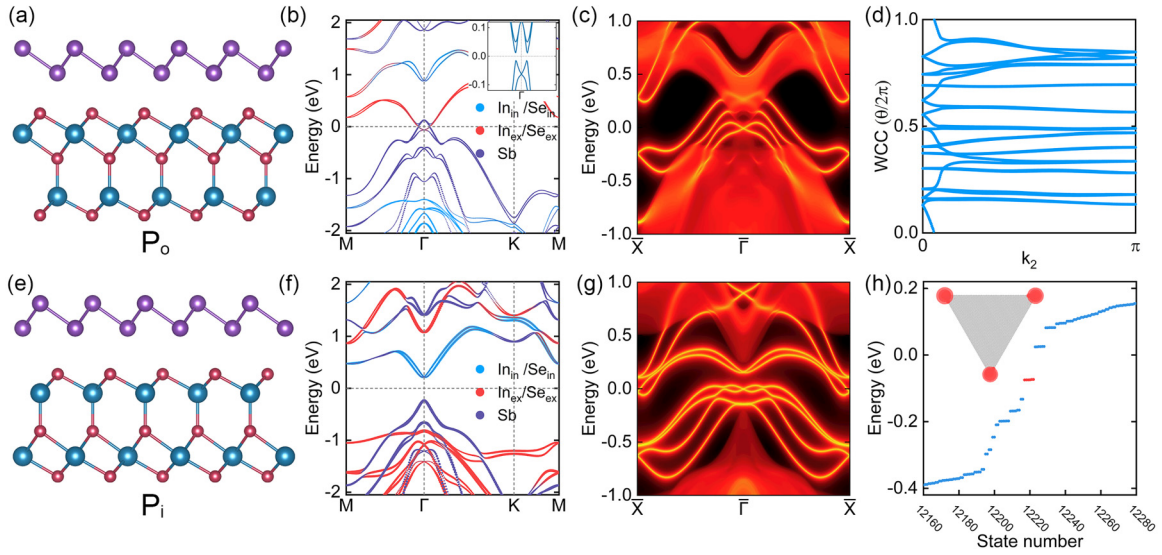


FIG. 8. Side views of the Sb/In₂Se₃ heterobilayer with (a) outward polarization P_o and (c) inward polarization P_i . Electronic band structures of the Sb/In₂Se₃ heterobilayer (b) under outward polarization with SOC, and (f) under inward polarization with SOC, respectively. The corresponding topological edge spectrum with (c) outward polarization and (g) inward polarization. (d) Evolution of WCC for Sb/In₂Se₃ heterobilayer with outward polarization. (h) Energy spectrum and charge distributions of triangle-shaped nanoflake for the heterobilayer with inward polarization, where the occupied corner states are marked by red dots.

thereby achieving a topological transition in the heterobilayer material.

APPENDIX B: DETAILED RESULTS FOR THE OTHER CANDIDATE MATERIALS

To achieve a ferroelectric topological phase transition, we looked for stable two-dimensional materials with lattice

parameters similar to In₂X₃ (X = S, Se) monolayers, constructed heterobilayers, and calculated their most stable stacking arrangement. Analyzing the band structure of both P_i and P_o phases, we identified four potential structures: MgAl₂Se₄/In₂S₃, Cu₂Br₂/In₂S₃, Sb/In₂Se₃, and Cu₂I₂/In₂Se₃ heterobilayers. Figures 7–9 show the detailed calculated results.

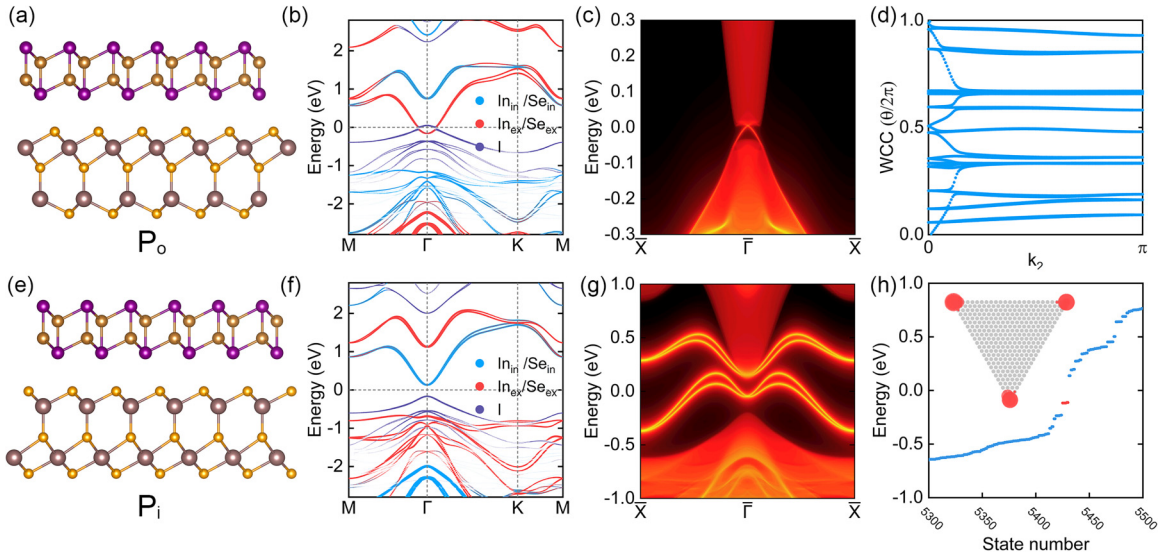


FIG. 9. Side views of the Cu₂I₂/In₂Se₃ heterobilayer with (a) outward polarization P_o and (c) inward polarization P_i . Electronic band structures of the Cu₂I₂/In₂Se₃ heterobilayer (b) under outward polarization with SOC, and (f) under inward polarization with SOC, respectively. The corresponding topological edge spectrum with (c) outward polarization and (g) inward polarization. (d) Evolution of WCC for Cu₂I₂/In₂Se₃ heterobilayer with outward polarization. (h) Energy spectrum and charge distributions of triangle-shaped nanoflake for the heterobilayer with inward polarization, where the occupied corner states are marked by red dots.

- [1] M. Z. Hasan and C. L. Kane, *Rev. Mod. Phys.* **82**, 3045 (2010).
- [2] X.-L. Qi and S.-C. Zhang, *Rev. Mod. Phys.* **83**, 1057 (2011).
- [3] A. Bansil, H. Lin, and T. Das, *Rev. Mod. Phys.* **88**, 021004 (2016).
- [4] C. L. Kane and E. J. Mele, *Phys. Rev. Lett.* **95**, 226801 (2005).
- [5] M. König, S. Wiedmann, C. Brüne, A. Roth, H. Buhmann, L. W. Molenkamp, X.-L. Qi, and S.-C. Zhang, *Science* **318**, 766 (2007).
- [6] B. A. Bernevig, T. L. Hughes, and S.-C. Zhang, *Science* **314**, 1757 (2006).
- [7] F. Schindler, Z. Wang, M. G. Vergniory, A. M. Cook, A. Murani, S. Sengupta, A. Y. Kasumov, R. Deblock, S. Jeon, I. Drozdov, H. Bouchiat, S. Guéron, A. Yazdani, B. A. Bernevig, and T. Neupert, *Nat. Phys.* **14**, 918 (2018).
- [8] W. A. Benalcazar, T. Li, and T. L. Hughes, *Phys. Rev. B* **99**, 245151 (2019).
- [9] M. J. Park, Y. Kim, G. Y. Cho, and S. B. Lee, *Phys. Rev. Lett.* **123**, 216803 (2019).
- [10] B. Liu, G. Zhao, Z. Liu, and Z. F. Wang, *Nano Lett.* **19**, 6492 (2019).
- [11] X.-L. Sheng, C. Chen, H. Liu, Z. Chen, Z.-M. Yu, Y. X. Zhao, and S. A. Yang, *Phys. Rev. Lett.* **123**, 256402 (2019).
- [12] Y. B. Choi, Y. Xie, C. Z. Chen, J. Park, S. B. Song, J. Yoon, B. J. Kim, T. Taniguchi, K. Watanabe, J. Kim, K. C. Fong, M. N. Ali, K. T. Law, and G. H. Lee, *Nat. Mater.* **19**, 974 (2020).
- [13] E. Lee, R. Kim, J. Ahn, and B.-J. Yang, *npj Quantum Mater.* **5**, 1 (2020).
- [14] S. K. Radha and W. R. L. Lambrecht, *Phys. Rev. B* **102**, 115104 (2020).
- [15] R. Noguchi, M. Kobayashi, Z. Jiang, K. Kuroda, T. Takahashi, Z. Xu, D. Lee, M. Hirayama, M. Ochi, T. Shirasawa *et al.*, *Nat. Mater.* **20**, 473 (2021).
- [16] J. Zeng, H. Liu, H. Jiang, Q.-F. Sun, and X. C. Xie, *Phys. Rev. B* **104**, L161108 (2021).
- [17] S. Qian, G.-B. Liu, C.-C. Liu, and Y. Yao, *Phys. Rev. B* **105**, 045417 (2022).
- [18] H. Mu, B. Liu, T. Hu, and Z. Wang, *Nano Lett.* **22**, 1122 (2022).
- [19] Aiyun Luo, Z. Song, and G. Xu, *npj Comput. Mater.* **8**, 26 (2022).
- [20] H. Mu, G. Zhao, H. Zhang, and Z. Wang, *npj Comput. Mater.* **8**, 82 (2022).
- [21] H. Huang and F. Liu, *Natl. Sci. Rev.* **9**, nwab170 (2022).
- [22] S.-Y. Xu, Y. Xia, L. A. Wray, S. Jia, F. Meier, J. H. Dil, J. Osterwalder, B. Slomski, A. Bansil, H. Lin, R. J. Cava, and M. Z. Hasan, *Science* **332**, 560 (2011).
- [23] C. Niu, P. M. Buhl, G. Bihlmayer, D. Wortmann, S. Blügel, and Y. Mokrousov, *Nano Lett.* **15**, 6071 (2015).
- [24] J. L. Collins, A. Tadich, W. Wu, L. C. Gomes, J. N. B. Rodrigues, C. Liu, J. Hellerstedt, H. Ryu, S. Tang, S.-K. Mo, S. Adam, S. A. Yang, M. S. Fuhrer, and M. T. Edmonds, *Nature (London)* **564**, 390 (2018).
- [25] B. Xu, L. X. Zhao, P. Marsik, E. Sheveleva, F. Lyzwa, Y. M. Dai, G. F. Chen, X. G. Qiu, and C. Bernhard, *Phys. Rev. Lett.* **121**, 187401 (2018).
- [26] J. Mutch, W.-C. Chen, P. Went, T. Qian, I. Z. Wilson, A. Andreev, C.-C. Chen, and J.-H. Chu, *Sci. Adv.* **5**, eaav9771 (2019).
- [27] C. Niu, N. Mao, X. Hu, B. Huang, and Y. Dai, *Phys. Rev. B* **99**, 235119 (2019).
- [28] C. Zhao, M. Hu, J. Qin, B. Xia, C. Liu, S. Wang, D. Guan, Y. Li, H. Zheng, J. Liu, and J. Jia, *Phys. Rev. Lett.* **125**, 046801 (2020).
- [29] H. Bai, X. Wang, W. Wu, P. He, Z. Xu, S. A. Yang, and Y. Lu, *Phys. Rev. B* **102**, 235403 (2020).
- [30] S. Dong, J.-M. Liu, S.-W. Cheong, and Z. Ren, *Adv. Phys.* **64**, 519 (2015).
- [31] L. Qi, S. Ruan, and Y.-J. Zeng, *Adv. Mater.* **33**, 2005098 (2021).
- [32] J.-J. Zhang, D. Zhu, and B. I. Yakobson, *Nano Lett.* **21**, 785 (2021).
- [33] Y. Zhou, D. Wu, Y. Zhu, Y. Cho, Q. He, X. Yang, K. Herrera, Z. Chu, Y. Han, M. C. Downer, H. Peng, and K. Lai, *Nano Lett.* **17**, 5508 (2017).
- [34] G. Kresse and J. Hafner, *Phys. Rev. B* **47**, 558 (1993).
- [35] G. Kresse and J. Furthmüller, *Phys. Rev. B* **54**, 11169 (1996).
- [36] J. P. Perdew, K. Burke, and M. Ernzerhof, *Phys. Rev. Lett.* **77**, 3865 (1996).
- [37] S. Grimme, J. Antony, S. Ehrlich, and H. Krieg, *J. Chem. Phys.* **132**, 154104 (2010).
- [38] A. A. Mostofi, J. R. Yates, Y.-S. Lee, I. Souza, D. Vanderbilt, and N. Marzari, *Comput. Phys. Commun.* **178**, 685 (2008).
- [39] Y. Ren, Z. Qiao, and Q. Niu, *Phys. Rev. Lett.* **124**, 166804 (2020).
- [40] C. Chen, Z. Song, J.-Z. Zhao, Z. Chen, Z.-M. Yu, X.-L. Sheng, and S. A. Yang, *Phys. Rev. Lett.* **125**, 056402 (2020).
- [41] J. C. Slater and G. F. Koster, *Phys. Rev.* **94**, 1498 (1954).
- [42] S. K. Radha and W. R. L. Lambrecht, *Phys. Rev. B* **101**, 235111 (2020).
- [43] L. Hu and X. Huang, *RSC Adv.* **7**, 55034 (2017).
- [44] J. Lu, J. Yao, J. Yan, W. Gao, L. Huang, Z. Zheng, M. Zhang, and J. Li, *Mater. Horiz.* **7**, 1427 (2020).
- [45] G. Zhang, K. Lu, Y. Wang, H. Wang, and Q. Chen, *Phys. Rev. B* **105**, 235303 (2022).
- [46] P. Zhao, Y. Ma, X. Lv, M. Li, B. Huang, and Y. Dai, *Nano Energy* **51**, 533 (2018).
- [47] W. Fang, K. Kuang, X. Xiao, H. Wei, Y. Chen, M. Li, and Y. He, *J. Alloys Compd.* **931**, 167586 (2023).
- [48] P. Li, W. Zhang, C. Liang, and X. C. Zeng, *Nanoscale* **11**, 19806 (2019).
- [49] W. Ding, J. Zhu, Z. Wang, Y. Gao, D. Xiao, Y. Gu, Z. Zhang, and W. Zhu, *Nat. Commun.* **8**, 14956 (2017).
- [50] F. Xue, J. Zhang, W. Hu, W.-T. Hsu, A. Han, S.-F. Leung, J.-K. Huang, Y. Wan, S. Liu, J. Zhang, J.-H. He, W.-H. Chang, Z. L. Wang, X. Zhang, and L.-J. Li, *ACS Nano* **12**, 4976 (2018).
- [51] J. Li, H. Li, X. Niu, and Z. Wang, *ACS Nano* **15**, 18683 (2021).
- [52] Z. Zhang, J. Nie, Z. Zhang, Y. Yuan, Y.-S. Fu, and W. Zhang, *Adv. Mater.* **34**, 2106951 (2022).
- [53] Y. Guo, X. Yu, Y. Zhang, X. Zhang, S. Yuan, Y. Li, S. A. Yang, and J. Wang, *ACS Nano* **16**, 11174 (2022).
- [54] J.-J. Zhang, Y. Zhang, and S. Dong, *Phys. Rev. Mater.* **2**, 126004 (2018).